The Phase Evolution and Degradation Modes of $R\bar{3}m$ $Li_xNi_{1-y-z}Co_yAl_zO_2$ Electrodes Cycled Near Complete Delithiation

Nicholas V. Faenza[1], Nathalie Pereira[1], David M. Halat[2], Julija Vinckeviciute[3], Lejandro Bruce[1], Maxwell D. Radin[3], Pinaki Mukherjee[4], Fadwa Badway[1], Anna Halajko[1], Frederic Cosandey[4], Clare P. Grey[2], Anton Van der Ven[3], and Glenn G. Amatucci[1]

[1]Energy Storage Research Group, Department of Materials Science and Engineering, Rutgers University, North Brunswick, New Jersey 08902, United States
[2]Department of Chemistry, University of Cambridge, Cambridge CB2 1EW, United Kingdom
[3]Materials Department, University of California Santa Barbara, Santa Barbara, California 93106-5050, United States
[4]Department of Materials Science and Engineering, Rutgers University, Piscataway, New Jersey 08854, United States

Supplemental Information

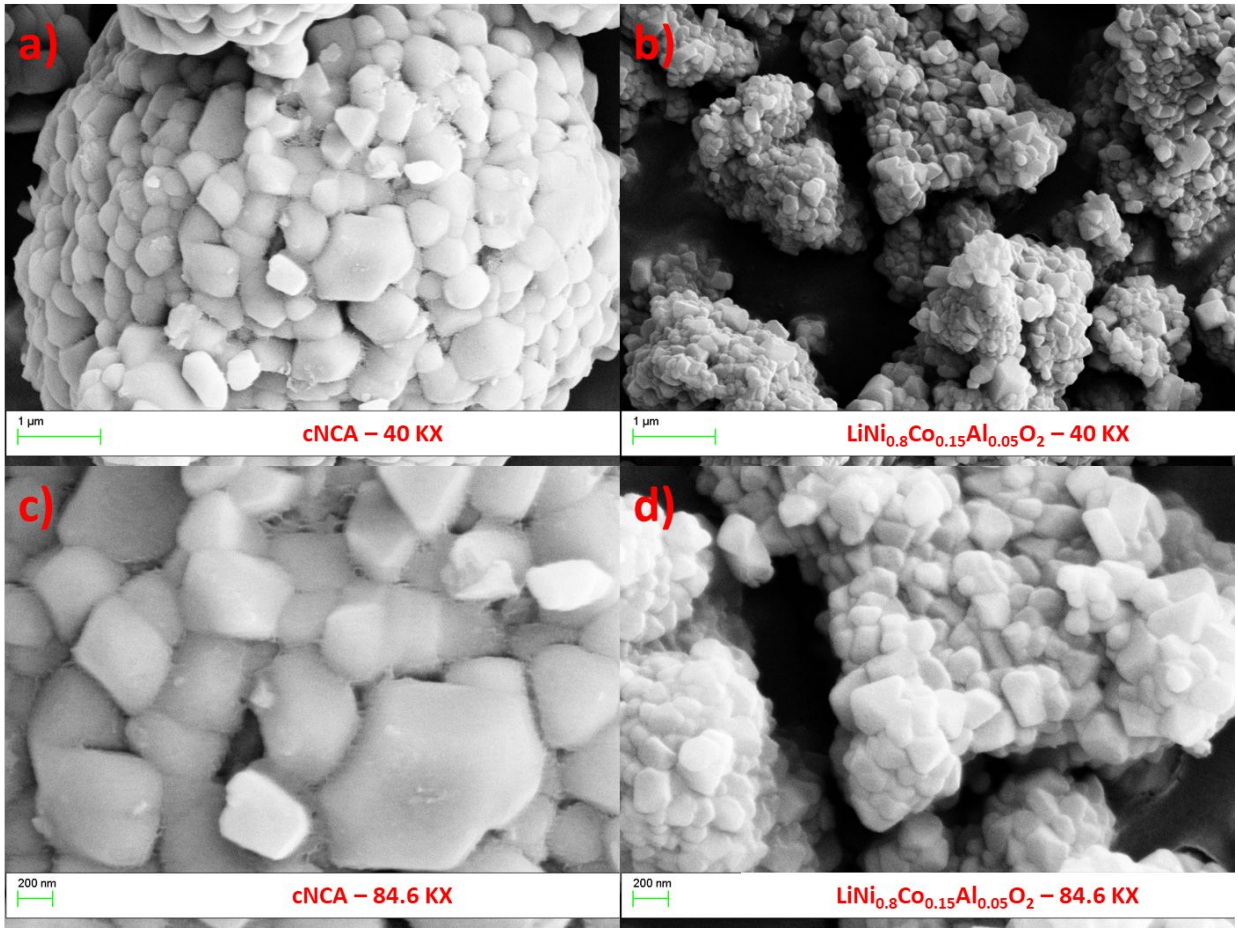

Figure S1: FESEM images representative of (a, c) cNCA and (b, d) $LiNi_{0.8}Co_{0.15}Al_{0.05}O_2$ particles at a magnification of (a-b) 40 KX and (c-d) 84.6 KX. Both materials were coated with a thin Au-layer to prevent charging by the electron beam.

Table SI: Rietveld calculated unit cell *a* and *c* lattice parameters and volume, Ni and/or Co occupancy, strain, and phase impurity percentage from the 12 h-XRD scans shown in Figure 1. Co_3O_4 is the impurity phase for group 1 materials (blue rows), while γ-$LiAlO_2$ is the impurity phase for the group 2 (red rows) and 3 (green rows) materials. No impurity phase was detected for multiple materials. For each Rietveld calculation the weighted profile residual (R_{wp}) and goodness-of-fit (GOF) are provided in the two rightmost columns. The standard deviation for all Rietveld calculated parameters are in parentheses. Since the error in the diffraction measurements is substantially larger than in the Rietveld calculations, the error of the parameters in the table are likely much greater than listed.

TA

Material	a (Å)	c (Å)	Volume (Å^3)	Ni, Co Occupancy on 3a Site	Strain (ε)	% Phase Impurity	Rwp
C. $LiCoO_2$	2.81663(13)	14.0578(17)	96.584(15)	0.01(7)	0.00(19)	0.0	1.84
$LiCoO_2$	2.81402(6)	14.0435(8)	96.308(7)	0.00125(5)	0.00(3)	3.9(6)	1.23
$LiCo_{0.95}Al_{0.05}O_2$	2.81409(5)	14.0584(6)	96.415(6)	0.01291(5)	0.00(3)	3.4(5)	0.89
$LiCo_{0.9}Al_{0.1}O_2$	2.81260(8)	14.0688(11)	96.385(10)	0.00(2)	0.000(2)	3.0(5)	1.54
$LiCo_{0.8}Al_{0.2}O_2$	2.80934(8)	14.1031(11)	96.395(9)	0.00125(1)	0.00(5)	3.3(6)	1.36
$LiNiO_2$	2.87907(3)	14.2027(3)	101.954(3)	0.0336(10)	0.000379(12)	0.0	2.67
$LiNi_{0.95}Al_{0.05}O_2$	2.87539(4)	14.2018(4)	101.687(4)	0.02567(6)	0.000583(19)	0.0	2.37
$LiNi_{0.9}Al_{0.1}O_2$	2.87441(7)	14.2044(9)	101.637(8)	0.03486(5)	0.00086(2)	0.0	3.31
$LiNi_{0.8}Al_{0.2}O_2$ (O)	2.86445(9)	14.2066(12)	100.949(11)	0.06661(7)	0.00170(4)	1.3(0)	3.12
$LiNi_{0.8}Al_{0.2}O_2$ (DO)	2.87281(14)	14.20196(18)	101.489(16)	0.08900(5)	0.00141(8)	2.0(1)	3.18
$LiNiO_2$	2.87907(3)	14.2027(3)	101.954(3)	0.0336(10)	0.000379(12)	0.0	2.67
$LiNi_{0.8}Co_{0.2}O_2$	2.86748(8)	14.1747(10)	100.936(9)	0.05101(5)	0.00080(6)	0.0	2.24
$LiNi_{0.8}Al_{0.2}O_2$ (O)	2.86445(9)	14.2066(12)	100.949(11)	0.06661(7)	0.00170(4)	1.3(0)	3.12
$LiNi_{0.8}Co_{0.15}Al_{0.05}O_2$	2.86615(7)	14.1802(9)	100.881(8)	0.02502(5)	0.00075(5)	0.0	1.88
C. $LiNi_{0.8}Co_{0.15}Al_{0.05}O_2$	2.86250(3)	14.1765(3)	100.598(3)	0.0130(10)	0.000419(13)	0.0	1.72

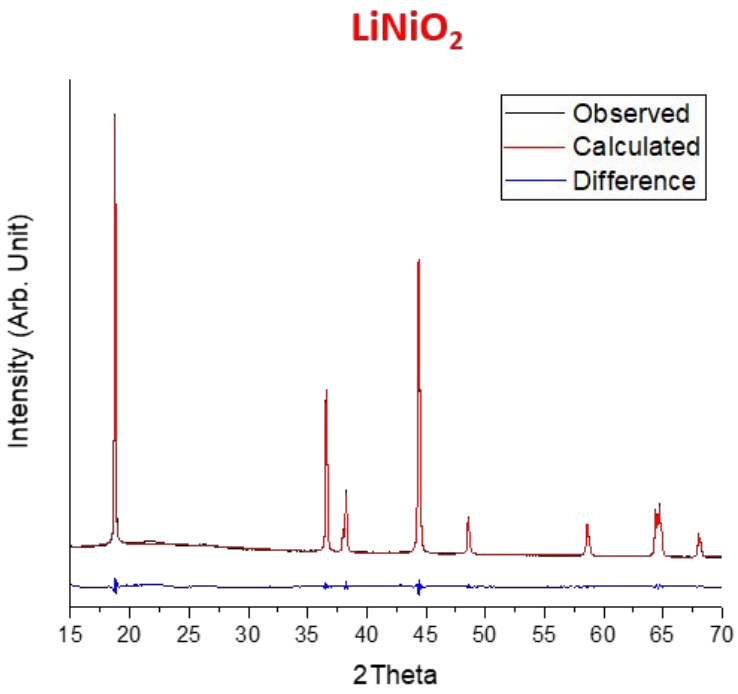

Figure S2: Representative observed (black) and Rietveld calculated (red) x-ray diffraction plots as well as the difference (blue) for $LiNiO_2$.

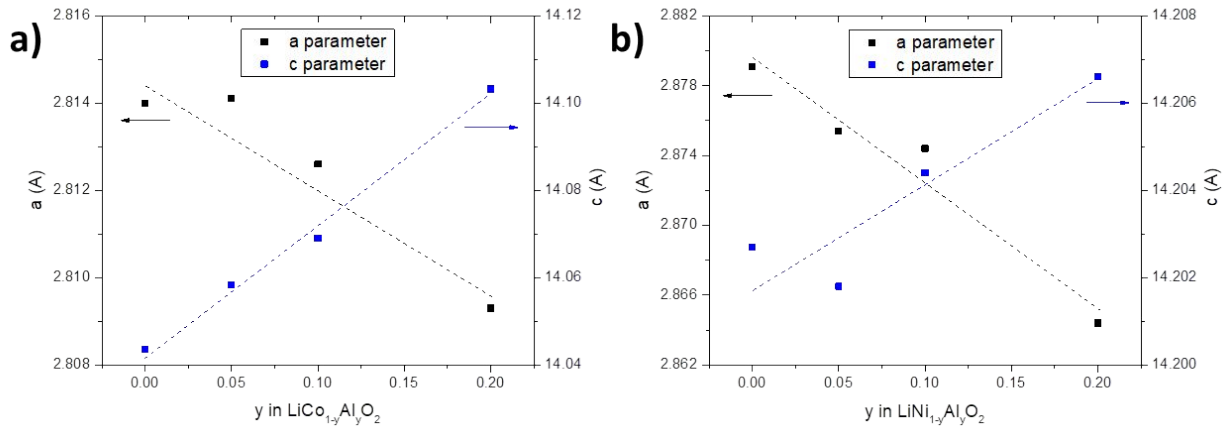

Figure S3: Rietveld calculated *a* (black) and *c* (blue) lattice parameters plotted as a function of Al content in (a) $LiCo_{1-y}Al_yO_2$ and (b) $LiNi_{1-y}Al_yO_2$ materials extracted from the XRD scans shown in Figure 1. $LiNi_{0.8}Al_{0.2}O_2$ (DO) is excluded because the disordered structure gave distorted lattice parameters. All lattice parameters were calculated based on an $R\bar{3}m$ unit cell.

Effect of Al substitution on the lattice parameters of $LiCoO_2$ and $LiNiO_2$:

The effect of Al-substitution on $LiCoO_2$ and $LiNiO_2$ is mainly associated with the difference in bond ionicity between Al-O and either Co-O or Ni-O rather than being based solely on a steric effect.[1–3] While

both Co^{3+} ($r_i(Co^{3+})$ = 0.525 Å) and Al^{3+} ($r_i(Al^{3+})$ = 0.53 Å) have smaller effective ionic radii than Ni^{3+} ($r_i(Ni^{3+})$ = 0.56 Å) and will thus contract the transition metal octahedra, only Al^{3+} is significantly more ionic than Ni^{3+}.[1,4] As such, the smaller and more ionic Al^{3+} ions create shorter Al-O bonds than the original Ni-O bonds, which contract the unit cell along the *a* axis, but enable an expansion of the *c* axis by elongating the LiO_6 octahedra.[1,3] The growth of the LiO_6 octahedra has been attributed to the Al ions which reduce the electron density around the oxygen atoms, and cause an increase in the Li-O bond length.[5] From comparison of the unit cell parameters for $LiNiO_2$, $LiNi_{0.8}Al_{0.2}O_2$ (O), $LiNi_{0.8}Co_{0.2}O_2$, and $LiNi_{0.8}Co_{0.15}Al_{0.05}O_2$ it was observed that 20% Al substitution contracts the *a* parameter similar to the 20% Co-substituted material, but elongates the *c* axis more. Intuitively, the $LiNi_{0.8}Co_{0.15}Al_{0.05}O_2$ material which has both Co and Al substitution has unit cell parameters between that of $LiNi_{0.8}Al_{0.2}O_2$ (O) and $LiNi_{0.8}Co_{0.2}O_2$.

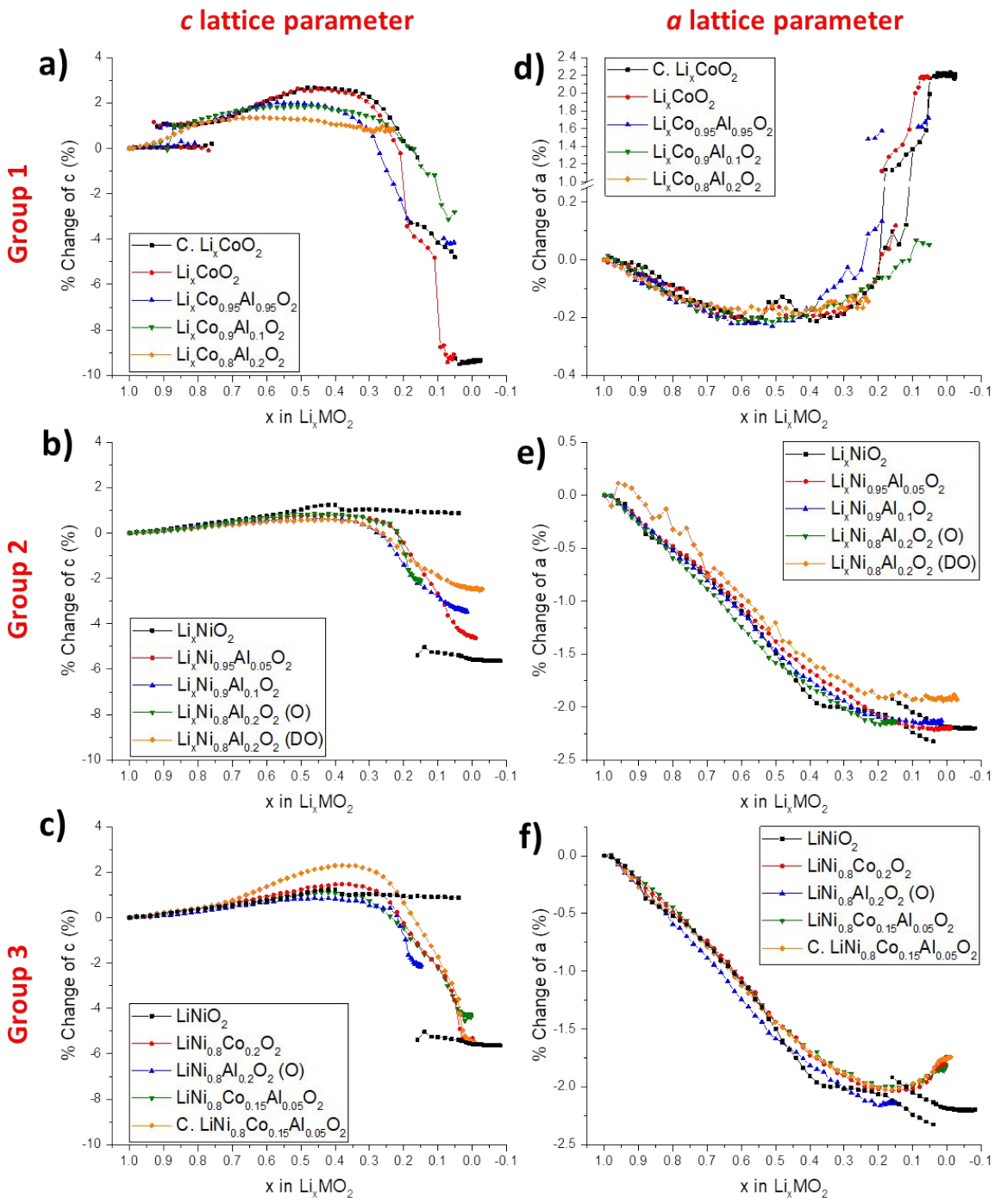

Figure S4: Percent change of the (a-c) *c* and (d-f) *a* lattice parameters calculated from *in-situ* XRD patterns for each material as a function of lithiation relative to the unit cell parameters in OCV (fully lithiated). The calculations are based on the *c* and *a* lattice parameters shown in Figures 4, 9, and 15.

Ex-situ XRD on the group 1 $LiCoO_2$-based materials:

Cells with a positive electrode from each group 1 $LiCoO_2$-based material were charged to 4.75 V using a PITT profile (10 mV steps, 1 mA/g cutoff). Once fully charged, the cells were disassembled in an Ar-filled glovebox and the positive electrode materials were retrieved to prepare *ex-situ* XRD samples. To temporarily prevent the hydrogen intercalation that rapidly occurs when highly delithiated materials are exposed to moisture, the positive electrode samples were sealed with a Kapton film and a short (30 min) XRD scan procedure was used. The *ex-situ* XRD results are shown in Figure S5, while the voltage profiles of the cells are presented in Figure S6. From the peak locations in Figure S5, it is evident that both cLCO and $LiCoO_2$ transformed to the O1 structure, and are in agreement with the *in-situ* XRD results. The *ex-situ* XRD patterns of the Al-substituted $LiCoO_2$ electrodes also support the *in-situ* experiments. As previously mentioned, even 5% Al substitution was sufficient to prevent the formation of the O1 structure, and the final (003) peak position maintained a larger d-spacing as more Al was substituted into the structure. Clearly, the Al concentration had a profound impact on the d-spacing evolution of the fully charged electrode materials. Adding Al to $LiCoO_2$ proportionally reduced the maximum degree of delithiation (Figure S6), thus limiting the phase transitions that occur at the higher states of charge.

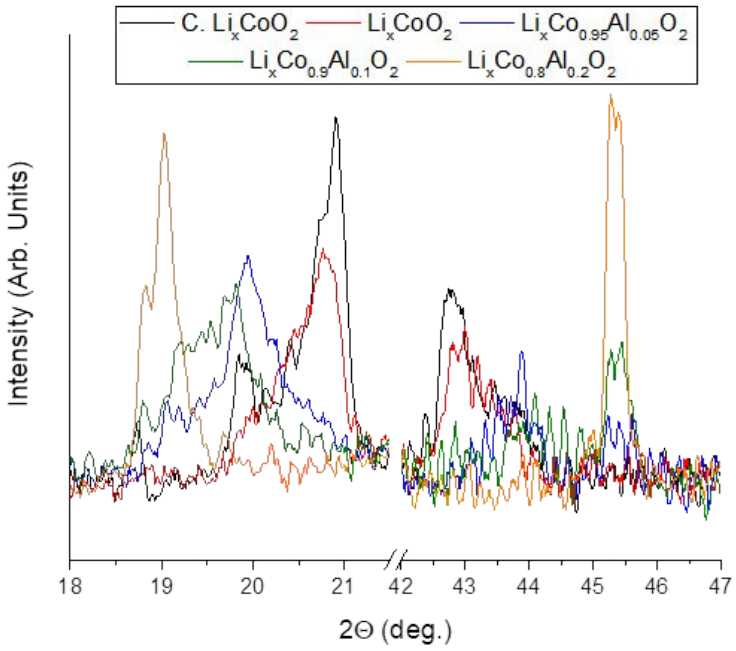

Figure S5: *Ex-situ* XRD scans of the positive electrode materials charged to 4.75 V (vs. Li metal) under PITT conditions (10 mV step, 1 mA/g cutoff) in the regions of the (003) Bragg peak (18-21.5°) and (104) peak (42-47°) for cLCO (black), $LiCoO_2$ (red), $LiCo_{0.95}Al_{0.05}O_2$ (blue), $LiCo_{0.9}Al_{0.1}O_2$ (green), and $LiCo_{0.8}Al_{0.2}O_2$ (orange). All cells were disassembled in an Ar-filled glovebox where the XRD samples were sealed with Kapton film to prevent contamination from the ambient atmosphere.

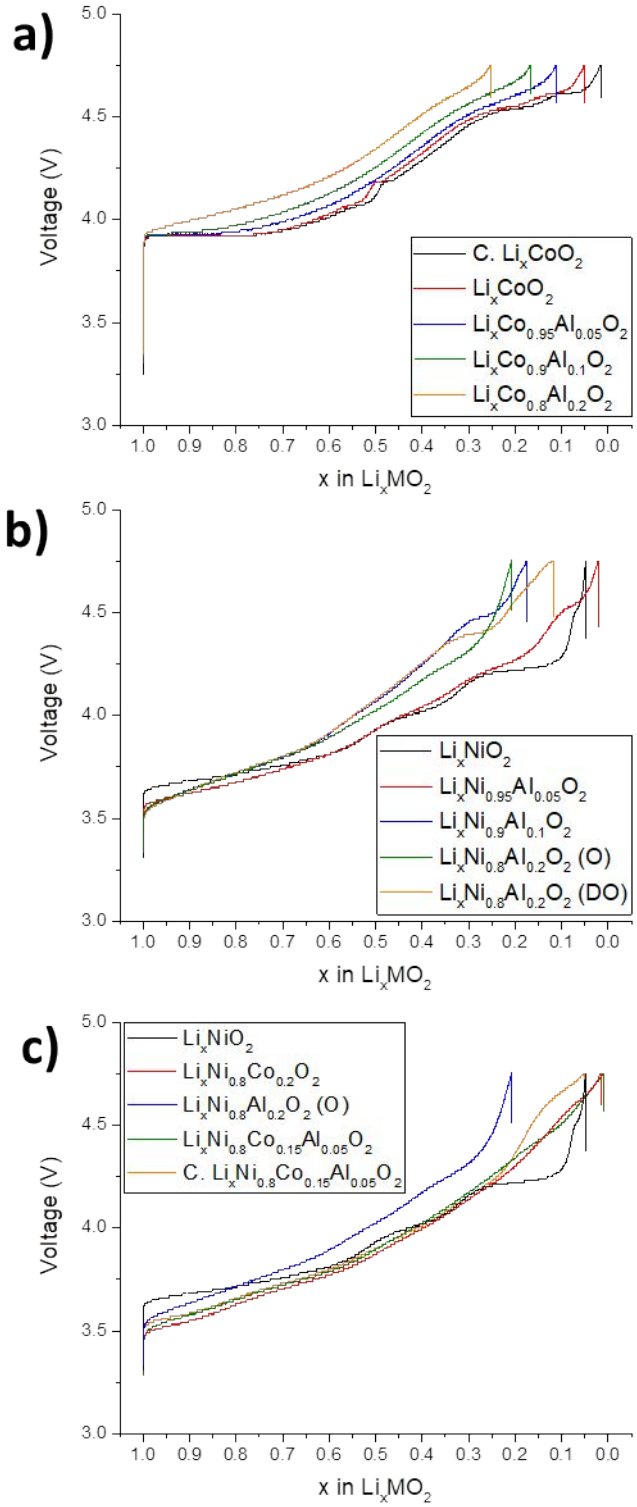

Figure S6: Voltage profiles as a function of lithium content for materials of (a) group 1, (b) group 2, and (c) group 3. Cells (vs. Li) were charged to 4.75 V under PITT conditions (10 mV step, 1 mA/g current cutoff) in a 24°C incubator.

Table SII: OCV, Li-content and Ni/Co oxidation percentage determined at the end of charge. Cells with positive electrode materials of group 1 (blue), 2 (red) and 3 (green) were charged versus Li metal to 4.75 V under a PITT protocol (10 mV step, 1 mA/g cutoff) and subjected to *ex-situ* XRD analysis (Figures S5 and S6). The tabulated OCV was recorded 1 h after the end of charge. The Ni, Co oxidation percentage was calculated from the measured charge capacity and theoretical capacity. Total oxidation values greater than 100% can be attributed to parasitic reactions at high potentials.

Properties at Full State of Charge			
Material	OCV (V) After 1 h	Final Lithiation x in Li_xMO_2	% Total Ni, Co Oxidation
C. $LiCoO_2$	4.59	0.02	98.37
$LiCoO_2$	4.58	0.05	94.89
$LiCo_{0.95}Al_{0.05}O_2$	4.65	0.11	93.55
$LiCo_{0.9}Al_{0.1}O_2$	4.68	0.17	92.55
$LiCo_{0.8}Al_{0.2}O_2$	4.65	0.25	93.48
$LiNiO_2$	4.47	0.05	95.30
$LiNi_{0.95}Al_{0.05}O_2$	4.50	0.02	103.12
$LiNi_{0.9}Al_{0.1}O_2$	4.54	0.17	91.69
$LiNi_{0.8}Al_{0.2}O_2$ (O)	4.61	0.21	99.11
$LiNi_{0.8}Al_{0.2}O_2$ (DO)	4.59	0.12	110.54
$LiNiO_2$	4.47	0.05	95.30
$LiNi_{0.8}Co_{0.2}O_2$	4.65	0.02	98.45
$LiNi_{0.8}Al_{0.2}O_2$ (O)	4.61	0.21	99.11
$LiNi_{0.8}Co_{0.15}Al_{0.05}O_2$	4.64	0.01	104.32
C. $LiNi_{0.8}Co_{0.15}Al_{0.05}O_2$	4.73	0.06	99.29

Table SIII: First cycle charge and discharge capacity (mAh/g), irreversible capacity loss (mAh/g and %), and theoretical capacity (mAh/g) for group 1 $LiCoO_2$-based materials. Cells were cycled versus Li metal by charging at 20 mA/g to V_{max} (4.5 or 4.75 V), maintaining a constant potential until the current dropped below 10 mA/g, and then discharging at 10 mA/g to 2.75 V. The theoretical capacity is based on electrochemically active Al.

Active Material	Vmax	First Cycle Charge Capacity (mAh/g)	First Cycle Discharge Capacity (mAh/g)	Irreversible Loss (mAh/g)	Irreversible Loss (%)	Theoretical Capacity (mAh/g)
C. $LiCoO_2$	4.5	199.1	194.7	4.4	2.2	273.9
C. $LiCoO_2$	4.5	198.7	194.1	4.6	2.3	273.9
C. $LiCoO_2$	4.75	257.0	246.4	10.6	4.1	273.9
C. $LiCoO_2$	4.75	257.8	247.0	10.8	4.2	273.9
$LiCoO_2$	4.5	191.8	183.4	8.4	4.4	273.9
$LiCoO_2$	4.5	193.0	182.3	10.7	5.6	273.9
$LiCoO_2$	4.75	252.0	235.1	17.0	6.7	273.9
$LiCoO_2$	4.75	249.0	232.0	17.0	6.8	273.9
$LiCo_{0.95}Al_{0.05}O_2$	4.5	187.6	164.8	22.8	12.1	278.4
$LiCo_{0.95}Al_{0.05}O_2$	4.5	187.8	164.8	23.0	12.3	278.4
$LiCo_{0.95}Al_{0.05}O_2$	4.75	237.3	202.1	35.2	14.8	278.4
$LiCo_{0.95}Al_{0.05}O_2$	4.75	238.8	202.8	36.0	15.1	278.4
$LiCo_{0.9}Al_{0.1}O_2$	4.75	180.0	149.7	30.2	16.8	283.1
$LiCo_{0.9}Al_{0.1}O_2$	4.75	183.3	152.2	31.1	17.0	283.1
$LiCo_{0.9}Al_{0.1}O_2$	4.5	224.5	179.6	44.9	20.0	283.1
$LiCo_{0.9}Al_{0.1}O_2$	4.5	225.2	179.0	46.2	20.5	283.1
$LiCo_{0.8}Al_{0.2}O_2$	4.5	168.9	121.4	47.4	28.1	293.0
$LiCo_{0.8}Al_{0.2}O_2$	4.5	169.3	121.6	47.6	28.1	293.0
$LiCo_{0.8}Al_{0.2}O_2$	4.75	193.5	132.4	61.1	31.6	293.0
$LiCo_{0.8}Al_{0.2}O_2$	4.75	194.8	133.4	61.4	31.5	293.0

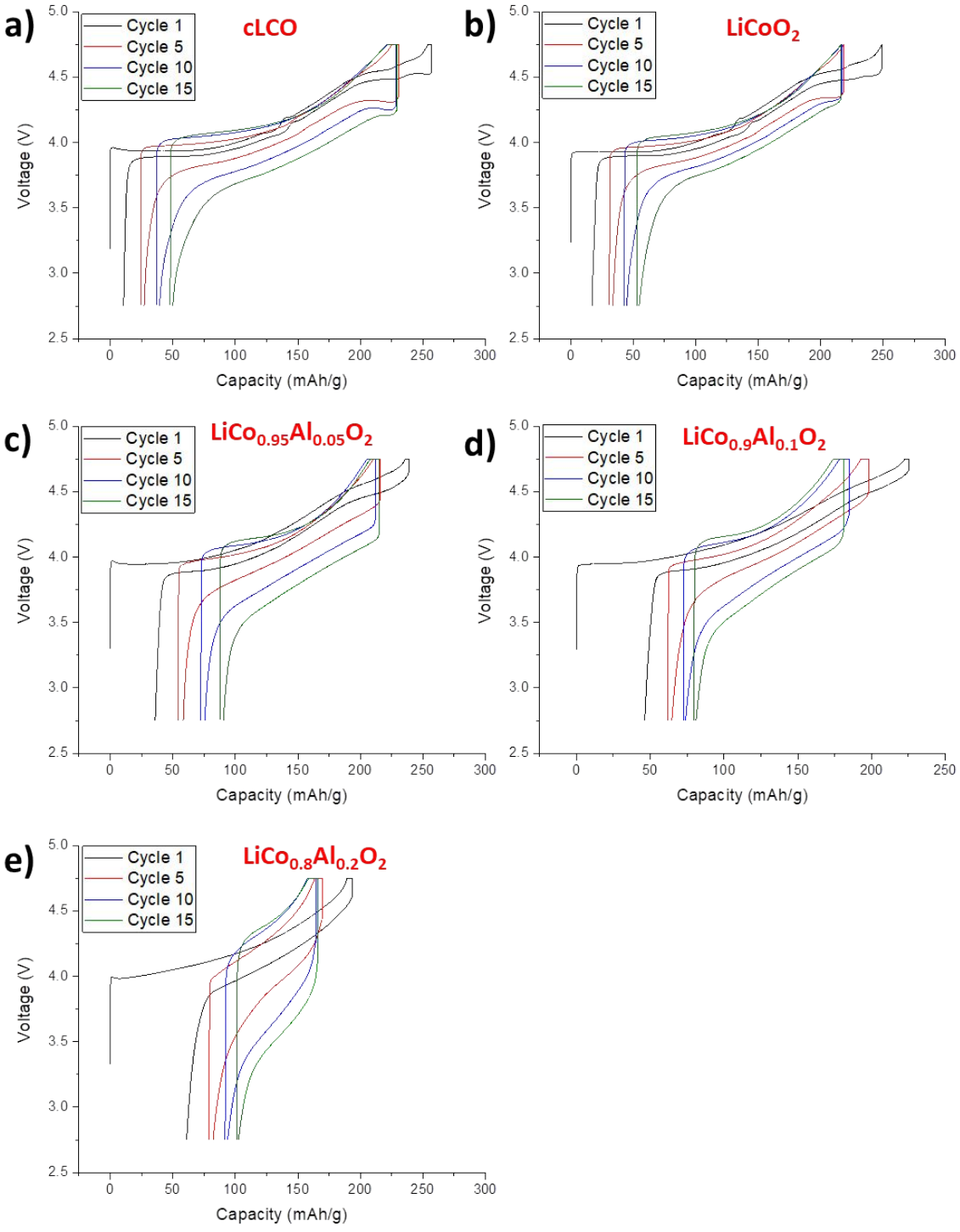

Figure S7: 1st, 5th, 10th and 15th cycle voltage profiles plotted as a function of capacity (mAh/g) for (a) cLCO, (b) $LiCoO_2$, (c) $LiCo_{0.95}Al_{0.05}O_2$, (d) $LiCo_{0.9}Al_{0.1}O_2$, and (e) $LiCo_{0.8}Al_{0.2}O_2$. Cells (vs. Li metal) were charged to 4.75 V at 20 mA/g, held at 4.75 V until the current decreased below 10 mA/g, and then discharged to 2.75 V at 10 mA/g, all at room temperature.

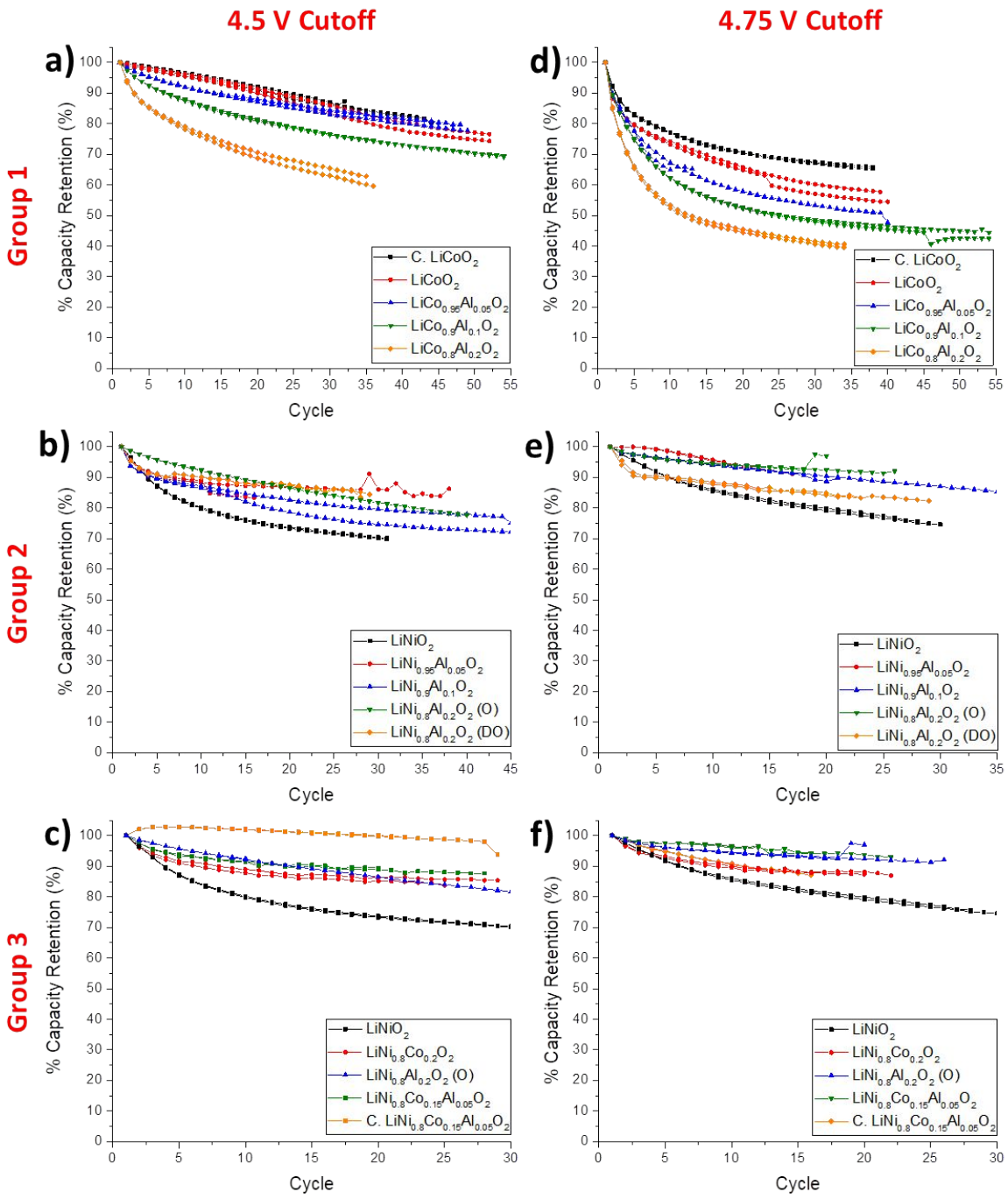

Figure S8: Discharge capacity retention (%) of group 1 (a, d), group 2 (b, e), and group 3 (c, f) positive materials upon cycling up to 4.5 V (a-c) and 4.75 V (d-f). Cells were cycled versus Li metal by charging at 20 mA/g to V_{max}, maintaining a constant potential until the current dropped below 10 mA/g, and then discharging at 10 mA/g to 2.75 V. Capacity retention was calculated by normalizing the discharge capacity of each cycle to the first cycle discharge capacity of the cell.

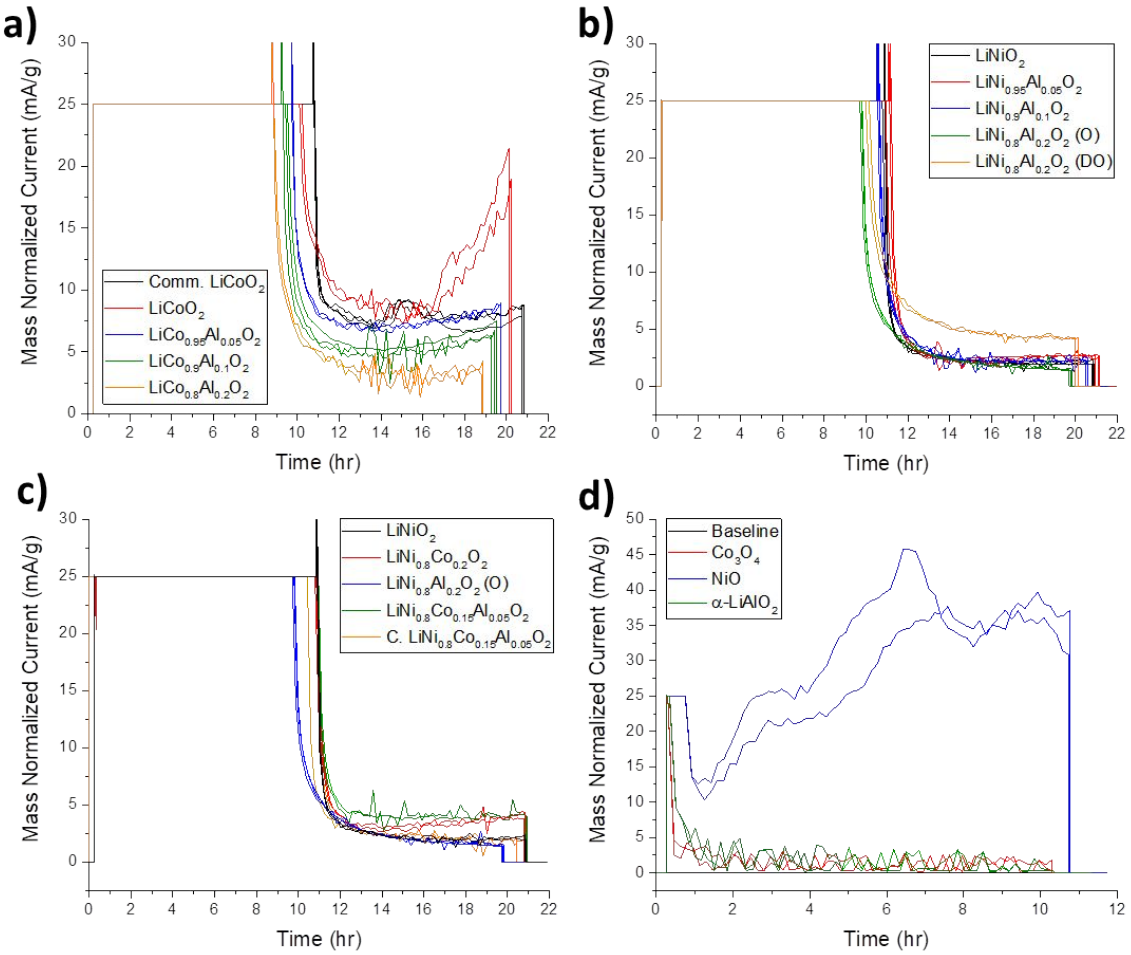

Figure S9: Current profiles of (a) group 1, (b) group 2, (c) group 3, and (d) reference materials used for ICP-OES measurements. Cells (vs. Li metal) were charged to 4.75 V at a constant current of 25 mA/g, and then held at 4.75 V for 10 h, at 60°C. The baseline cell, which consists of all cell parts except for a positive electrode, was used to determine that all of the Ni or Co measured was from the positive electrode.

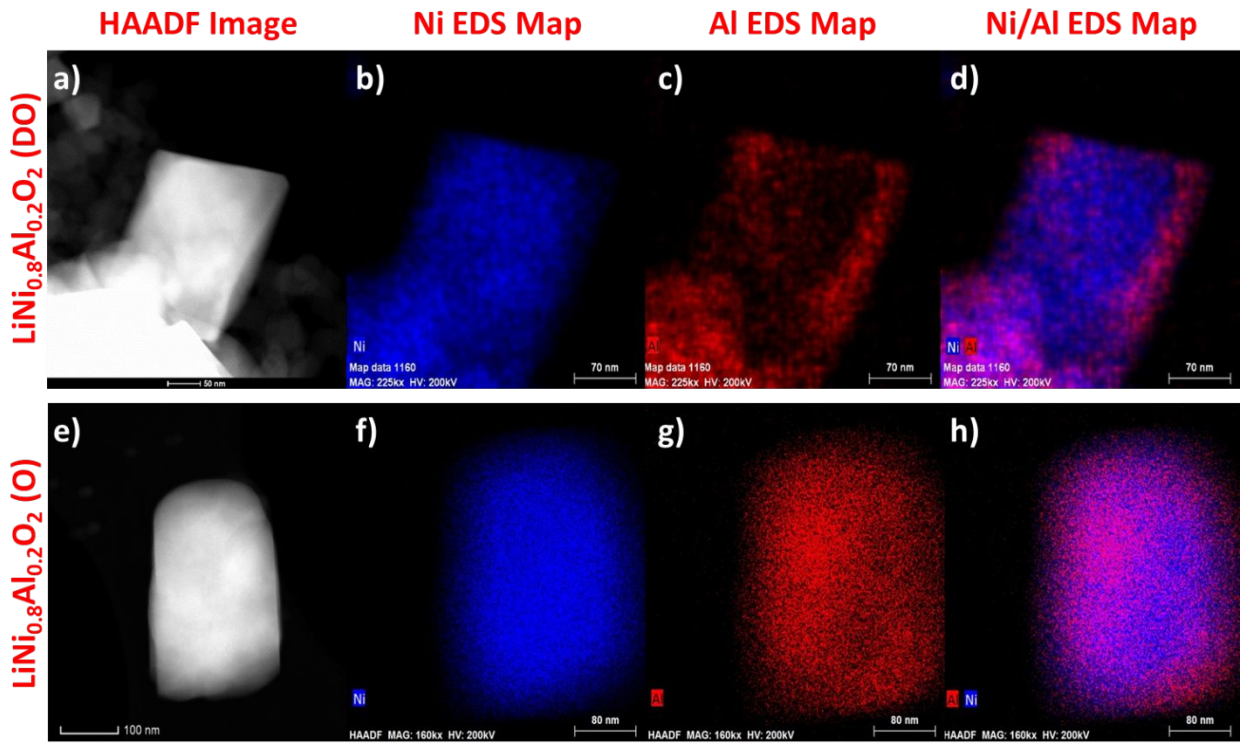

Figure S10: Comparison of representative particles of (a-d) $LiNi_{0.8}Al_{0.2}O_2$ (DO) and (e-h) $LiNi_{0.8}Al_{0.2}O_2$ (O) using (a, e) HAADF imaging and EDS mapping of the (b, f) Ni, (c, g) Al, and (d, h) both Ni and Al signals.

Crystal structures for fully delithiated layered oxides:

It has been well established that when fully delithiated, Li_xCoO_2 has a structural transition to the $P\bar{3}m1$ space group which is denoted as the O1 structure. In this O1 configuration (Figure S10 (c, f)), the Co atoms from neighboring layers align directly above one another, and only two unique oxygen positions are present which gives the structure its AB AB packing sequence. However, to our knowledge this structure has not been observed in NiO_2 (fully delithiated Li_xNiO_2), and is generally considered to be a consequence of the additional divalent transition metal in the Li 3a site that is prevalent for $LiNiO_2$-based materials. Instead, a structural transition from the original rhombohedral ($R\bar{3}m$) to a monoclinic (C2/m) phase has been observed.[6,7]

A comparison of the Rietveld determined crystal structures of delithiated NiO_2 in C2/m and $R\bar{3}m$ space groups as well as CoO_2 in a $P\bar{3}m1$ structure is presented in Figure S11. Using *in-situ* X-ray measurements with a high-resolution synchrotron beam line, Tarascon *et al.* determined that the structure of NiO_2 was C2/m and claimed that this structure was a distortion of the CdI_2 structure and could thus be considered to be O1.[7] While it is true that NiO_2 in the C2/m space group (Figure S11 (a, d)) does have an AB stacking sequence similar to CoO_2 in the $P\bar{3}m1$ space group (Figure S11 (c, f)), there are substantial differences between the two structures. The necessary distortion to the $P\bar{3}m1$ structure to form C2/m causes a substantial increase in the β angle from 90° to ~126°. Relative to the (001) plane, this forces the neighboring NiO_2 (or CoO_2) slabs to shift and offset themselves. As a result of this shift, the interlayer octahedral environment (3a site in $R\bar{3}m$) is changed from face sharing in $P\bar{3}m1$ to edge sharing in C2/m.

The specific environment of this octahedral position is critically relevant for insertion materials, because it is this site which will accommodate Li ions upon reduction of the material. Because the interlayer octahedral sites in C2/m have edge sharing with the adjacent interlayer octahedral sites, from the perspective of Li^+ intercalation the structure more closely resembles R$\bar{3}$m (O3) than P$\bar{3}$m1 (O1). Thus, in the context of electrochemical positive electrode materials it is misleading to consider the C2/m structure as an O1-type structure when it can be more acutely described as O3-type.

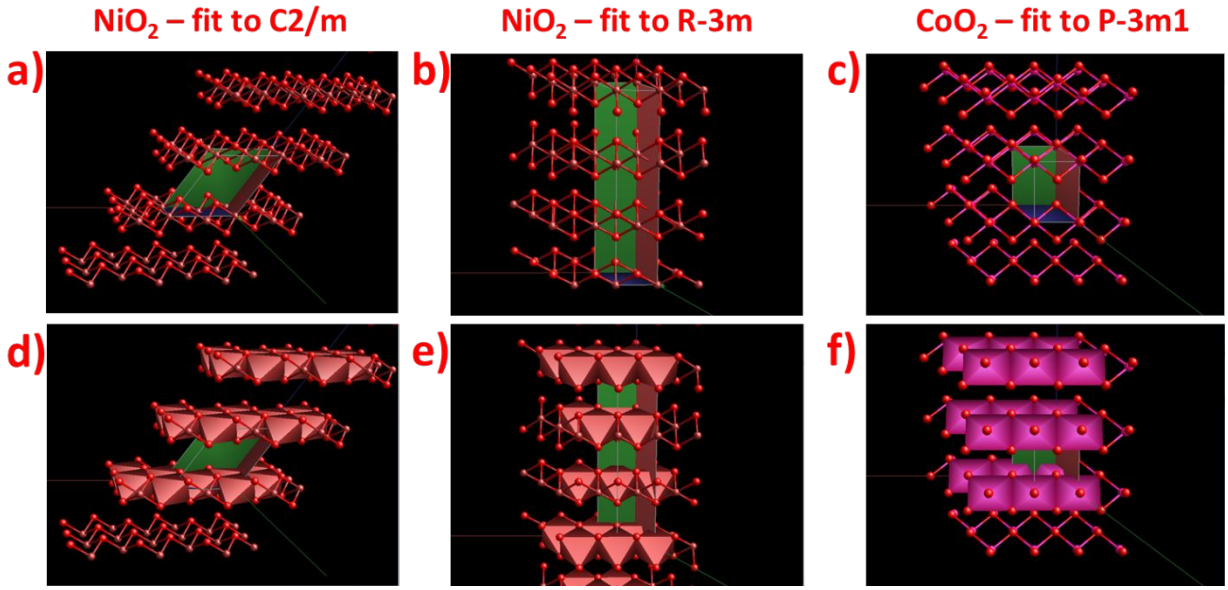

Figure S11: Schematization of the Rietveld calculated crystal structures (a-c) with and (d-f) without the transition metal octahedra for (a, d) NiO_2 fit to a C2/m space group, (d, e) NiO_2 fit to R$\bar{3}$m, and (c, f) CoO_2 fit to P$\bar{3}$m1. O, Ni and Co atoms are represented by red, maroon, and pink balls, respectively. All structures are oriented so that the *a* axis (red line) is directed to the left, and the *b* axis (green line) is indirectly positioned towards the reader.

Table SIV: First cycle charge and discharge capacity (mAh/g), irreversible capacity loss (mAh/g and %), and theoretical capacity (mAh/g) for group 2 $LiNiO_2$-based materials. Cells were cycled versus Li metal by charging at 20 mA/g to V_{max} (4.5 or 4.75 V), maintaining a constant potential until the current dropped below 10 mA/g, and then discharging at 10 mA/g to 2.75 V. The theoretical capacity is based on electrochemically active Al.

Material	V_{max}	First Cycle Charge Capacity (mAh/g)	First Cycle Discharge Capacity (mAh/g)	Irreversible Loss (mAh/g)	Irreversilbe Loss (%)	Theoretical Capacity (mAh/g)
$LiNiO_2$	4.5	255.2	217.8	37.4	14.7	274.5
$LiNiO_2$	4.5	255.3	218.3	37.0	14.5	274.5
$LiNiO_2$	4.75	265.5	221.9	43.6	16.4	274.5
$LiNiO_2$	4.75	262.4	220.1	42.3	16.1	274.5
$LiNi_{0.95}Al_{0.05}O_2$	4.5	233.7	187.4	46.3	19.8	279.1
$LiNi_{0.95}Al_{0.05}O_2$	4.5	241.3	195.4	45.9	19.0	279.1
$LiNi_{0.95}Al_{0.05}O_2$	4.75	255.7	214.5	41.2	16.1	279.1
$LiNi_{0.95}Al_{0.05}O_2$	4.75	237.4	197.5	39.8	16.8	279.1
$LiNi_{0.9}Al_{0.1}O_2$	4.5	205.8	164.6	41.2	20.0	283.7
$LiNi_{0.9}Al_{0.1}O_2$	4.5	206.6	162.9	43.7	21.1	283.7
$LiNi_{0.9}Al_{0.1}O_2$	4.75	243.1	195.1	48.1	19.8	283.7
$LiNi_{0.9}Al_{0.1}O_2$	4.75	248.4	198.1	50.3	20.2	283.7
$LiNi_{0.8}Al_{0.2}O_2$ (O)	4.5	194.4	161.1	33.3	17.1	293.6
$LiNi_{0.8}Al_{0.2}O_2$ (O)	4.5	196.5	162.9	33.6	17.1	293.6
$LiNi_{0.8}Al_{0.2}O_2$ (O)	4.75	232.9	191.4	41.5	17.8	293.6
$LiNi_{0.8}Al_{0.2}O_2$ (O)	4.75	232.5	190.0	42.5	18.3	293.6
$LiNi_{0.8}Al_{0.2}O_2$ (DO)	4.5	197.0	165.7	31.4	15.9	293.6
$LiNi_{0.8}Al_{0.2}O_2$ (DO)	4.5	196.6	166.1	30.5	15.5	293.6
$LiNi_{0.8}Al_{0.2}O_2$ (DO)	4.75	240.0	179.4	60.7	25.3	293.6
$LiNi_{0.8}Al_{0.2}O_2$ (DO)	4.75	229.1	174.5	54.6	23.8	293.6

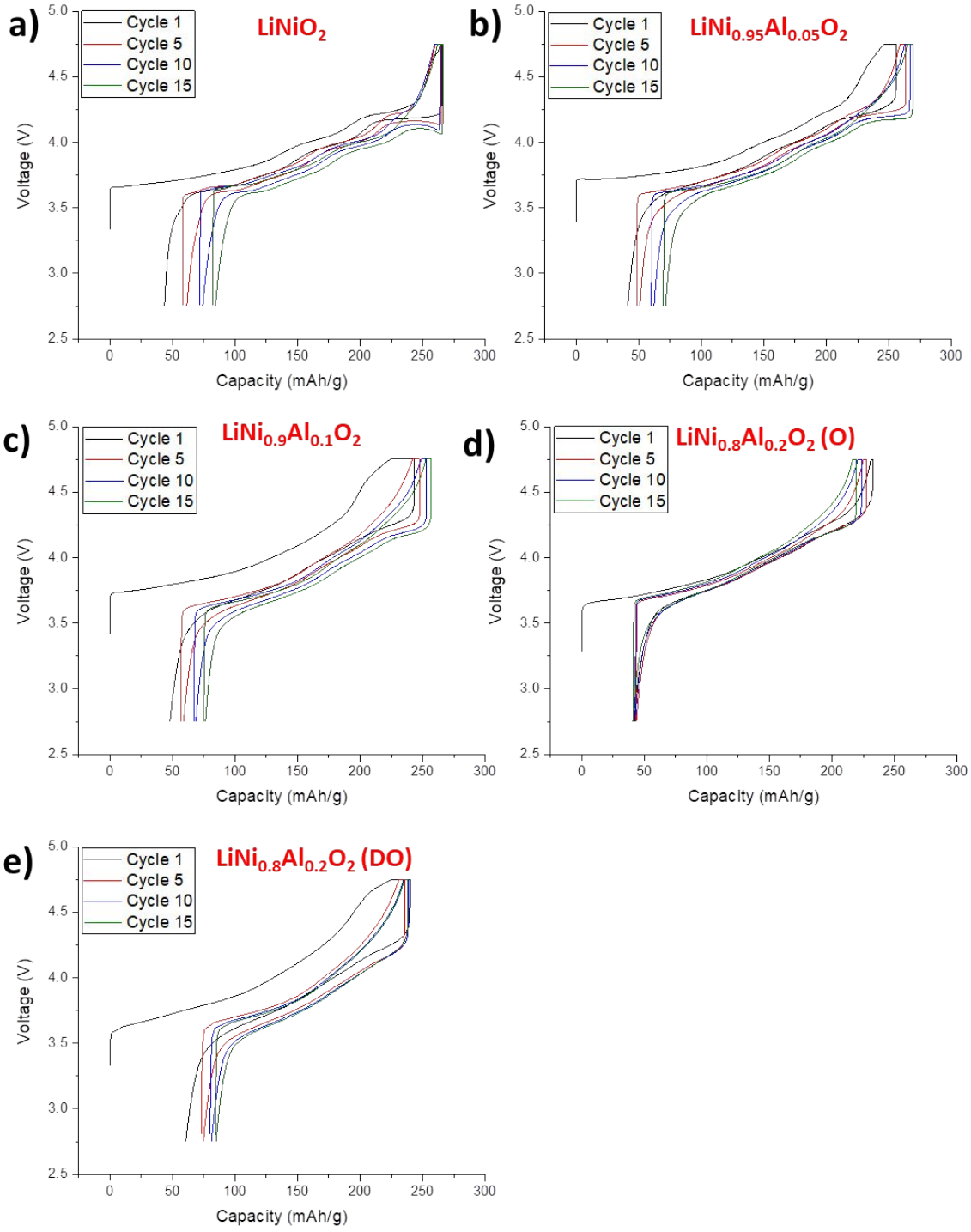

Figure S12: 1st, 5th, 10th and 15th cycle voltage profiles plotted as a function of capacity (mAh/g) for (a) $LiNiO_2$, (b) $LiNi_{0.95}Al_{0.05}O_2$, (c) $LiNi_{0.9}Al_{0.1}O_2$, (d) $LiNi_{0.8}Al_{0.2}O_2$ (O), and (e) $LiNi_{0.8}Al_{0.2}O_2$ (DO). Cells (vs. Li metal) were charged to 4.75 V at 20 mA/g, held at 4.75 V until the current decreased below 10 mA/g, and then discharged at 10 mA/g to 2.75 V, all at room temperature.

Table SV: First cycle charge and discharge capacity (mAh/g), irreversible capacity loss (mAh/g and %), and theoretical capacity (mAh/g) for group 3 $LiNiO_2$-based materials. Cells were cycled versus Li metal by charging at 20 mA/g to V_{max} (4.5 or 4.75 V), maintaining a constant potential until the current dropped below 10 mA/g, and then discharging at 10 mA/g to 2.75 V. The theoretical capacity is based on electrochemically active Al.

Active Material	Vmax	First Cycle Charge Capacity (mAh/g)	First Cycle Discharge Capacity (mAh/g)	Irreversible Loss (mAh/g)	Irreversible Loss (%)	Theoretical Capacity (mAh/g)
$LiNiO_2$	4.5	255.2	217.8	37.4	14.7	274.5
$LiNiO_2$	4.5	255.3	218.3	37.0	14.5	274.5
$LiNiO_2$	4.75	265.5	221.9	43.6	16.4	274.5
$LiNiO_2$	4.75	262.4	220.1	42.3	16.1	274.5
$LiNi_{0.8}Co_{0.2}O_2$	4.5	238.6	211.8	26.8	11.2	274.4
$LiNi_{0.8}Co_{0.2}O_2$	4.5	230.8	205.7	25.1	10.9	274.4
$LiNi_{0.8}Co_{0.2}O_2$	4.75	251.2	224.4	26.8	10.7	274.4
$LiNi_{0.8}Co_{0.2}O_2$	4.75	252.1	225.9	26.2	10.4	274.4
$LiNi_{0.8}Al_{0.2}O_2(O)$	4.5	194.4	161.1	33.3	17.1	293.6
$LiNi_{0.8}Al_{0.2}O_2(O)$	4.5	196.5	162.9	33.6	17.1	293.6
$LiNi_{0.8}Al_{0.2}O_2(O)$	4.75	232.9	191.4	41.5	17.8	293.6
$LiNi_{0.8}Al_{0.2}O_2(O)$	4.75	232.5	190.0	42.5	18.3	293.6
$LiNi_{0.8}Co_{0.15}Al_{0.05}O_2$	4.5	224.8	209.2	15.6	6.9	279.0
$LiNi_{0.8}Co_{0.15}Al_{0.05}O_2$	4.5	224.9	208.9	16.1	7.1	279.0
$LiNi_{0.8}Co_{0.15}Al_{0.05}O_2$	4.75	241.1	214.7	26.5	11.0	279.0
$LiNi_{0.8}Co_{0.15}Al_{0.05}O_2$	4.75	247.5	219.1	28.4	11.5	279.0
C. $LiNi_{0.8}Co_{0.15}Al_{0.05}O_2$	4.5	220.6	200.8	19.8	9.0	279.0
C. $LiNi_{0.8}Co_{0.15}Al_{0.05}O_2$	4.5	220.3	200.7	19.6	8.9	279.0
C. $LiNi_{0.8}Co_{0.15}Al_{0.05}O_2$	4.75	253.0	234.6	18.4	7.3	279.0
C. $LiNi_{0.8}Co_{0.15}Al_{0.05}O_2$	4.75	254.8	236.1	18.6	7.3	279.0

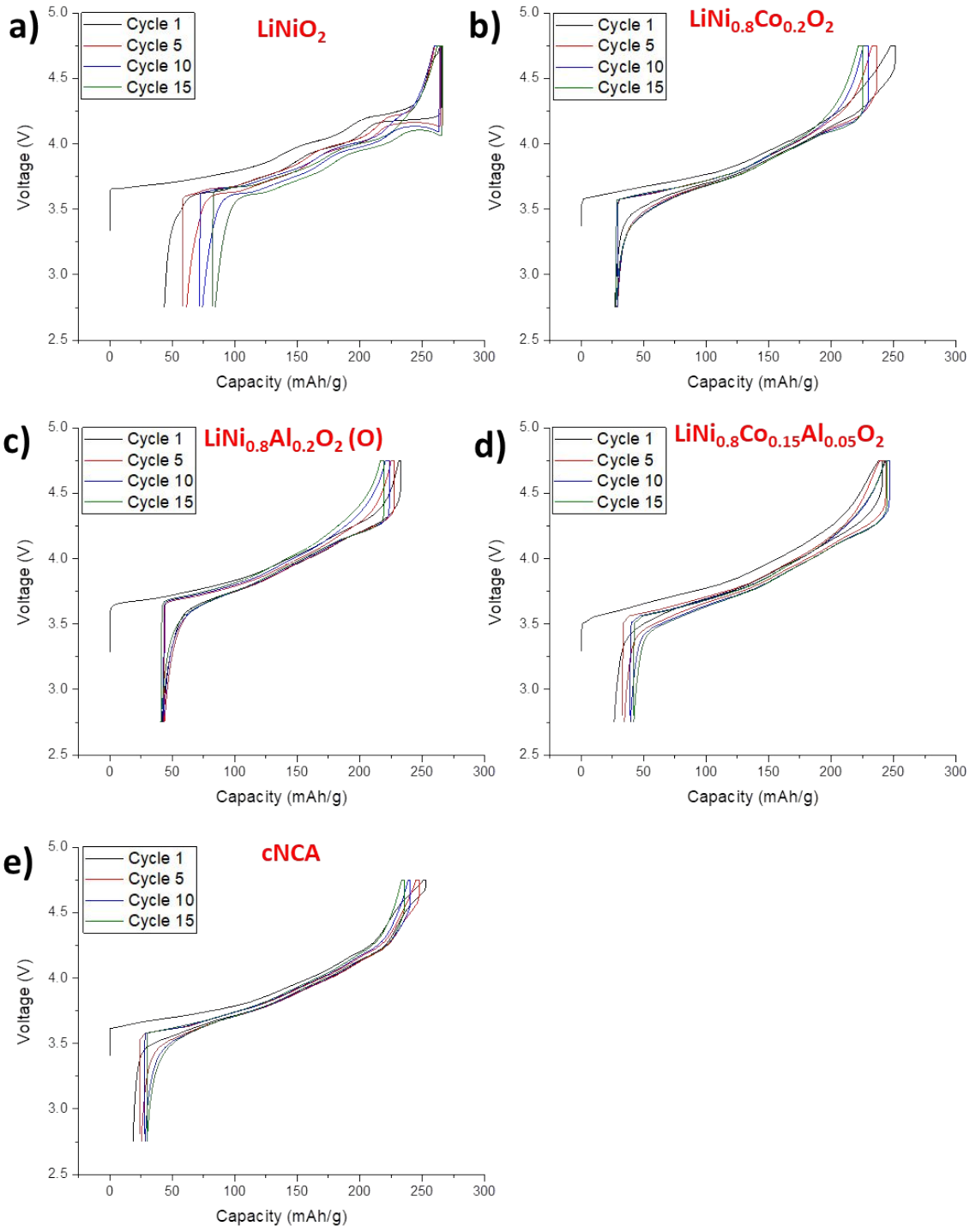

Figure S13: 1st, 5th, 10th and 15th cycle voltage profiles plotted as a function of capacity (mAh/g) for (a) $LiNiO_2$, (b) $LiNi_{0.8}Co_{0.2}O_2$, (c) $LiNi_{0.8}Al_{0.2}O_2$ (O), (d) $LiNi_{0.8}Co_{0.15}Al_{0.05}O_2$, and (e) cNCA. Cells (vs. Li metal) were charged to 4.75 V at 20 mA/g, held at 4.75 V until the current decreased below 10 mA/g, and then discharged at 10 mA/g to 2.75 V, all at room temperature.

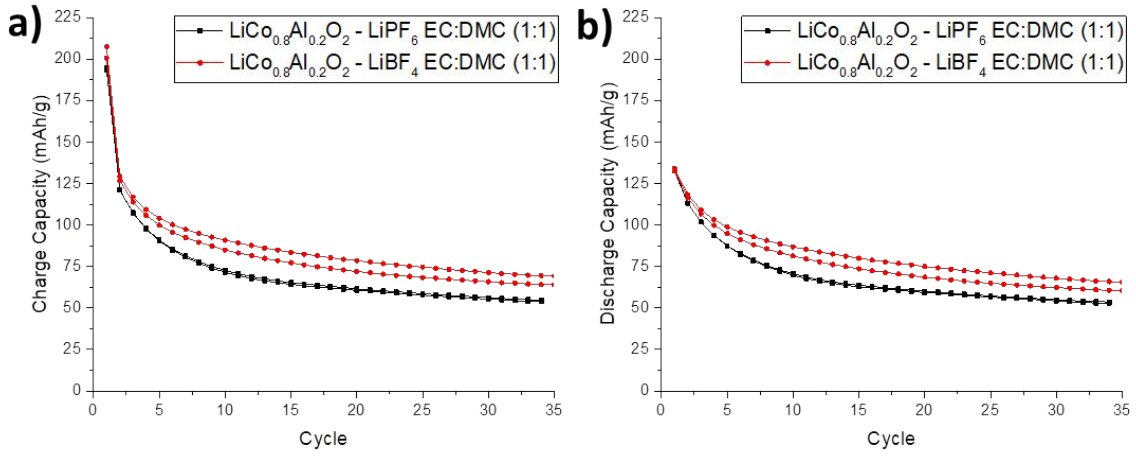

Figure S14: (a) Charge and (b) discharge capacities as a function of cycle number for $LiCo_{0.8}Al_{0.2}O_2$. Duplicate cells were cycled versus Li metal negative electrodes using either 1M $LiPF_6$ EC:DMC (1:1) (black), or 1M $LiBF_4$ EC:DMC (1:1) (red). Electrodes were charged at 20 mA/g to 4.75 V, held at a constant potential until the current decreased below 10 mA/g, and then discharged at 10 mA/g to 2.75 V, all at room temperature.

Theoretical Calculations for Transition Metal Migration:

The structures used in DFT calculations for the Li-Al defect in $LiAlM_{15}O_{32}$ (M = Ni or Co) are illustrated in Figure S15. The figure explicitly shows the in-plane octahedral ordering with an Al in the transition metal layer and an adjacent residual Li, as well as the Li-Al dumbbell configuration. Configurations with Li in other sites were higher energy. The defect energy is calculated by subtracting the in-plane octahedral configuration from the dumbbell, such that positive values indicate the former to be stable.

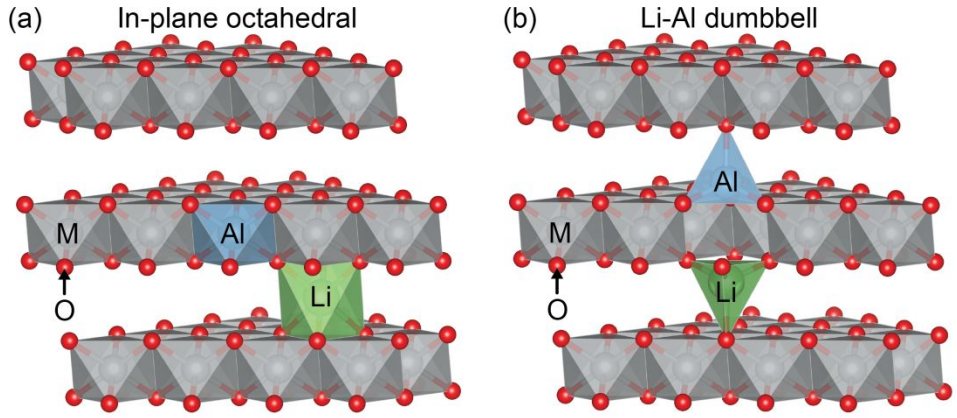

Figure S15: (a) In-plane octahedral and (b) Li-Al dumbbell configurations for determining dumbbell formation energy, with formula unit $LiAlM_{15}O_{32}$ (M = Co or Ni). Some mirror-image Li and Al atoms not shown for clarity. A Li-Al dumbbell is unstable in $LiNi_{15}AlO_{32}$, but the two configurations have very similar energies in $LiCo_{15}AlO_{32}$.[8]

Interlayer migration is most detrimental when it is not reversible. Figure S16 shows a possible migration pathway for the metal ions that may result in the irreversible migration of Al from the transition metal layer to the Li layer. As long as dumbbells can form in the structure, the stability of Li-Li dumbbells can

drive Al away from the vacancy in the transition metal layer and cause it to become stuck in the Li layer even upon relithiation.

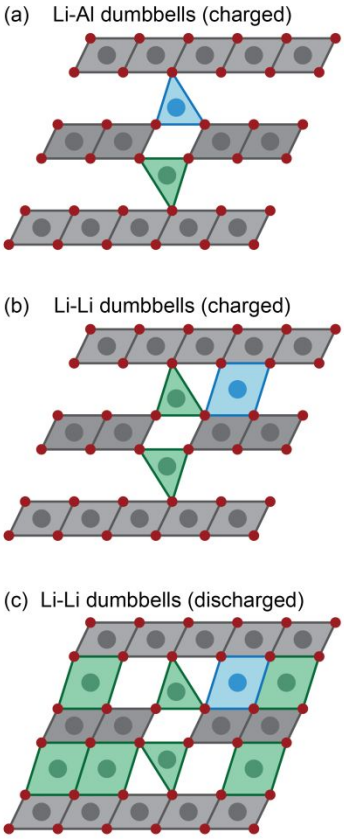

Figure S16: Possible irreversible migration pathway of Al that could result in capacity loss and/or material degradation: (a) Li-Al and (b) Li-Li dumbbell configurations in the charged state, and (c) Li-Li dumbbell configuration in the discharged state.

^{27}Al solid-state NMR spectroscopy:

Local Al environments present in the $LiCo_{0.8}Al_{0.2}O_2$ and $LiNi_{0.8}Al_{0.2}O_2$ (O) samples were identified by ^{27}Al solid-state magic-angle spinning (MAS) NMR spectroscopy. All samples were packed into 1.3 mm MAS rotors in an Ar-filled glovebox, without exposure to the ambient atmosphere. The ^{27}Al NMR spectra for the pristine material and the cycled $LiCo_{0.8}Al_{0.2}O_2$ samples with differing upper cutoff potentials (4.2 V, 4.5 V, and 4.75 V) are presented in Figure S17, with fitted spectral deconvolutions as described in the caption. The multiple features at lower frequencies (between 27 and 62 ppm) in Figure S17 represent octahedral Al sites with differing numbers of Co^{3+} neighbors, in agreement with previous studies; lower shifts indicate more neighboring Co^{3+}.[9] The spectral deconvolution clearly shows the development of another signal at ~70 ppm (broad, red peak) with increasing upper voltage cutoff, which is attributed to tetrahedral Al (see later).

Due to the increased internal impedance when charging to higher potentials and the increased irreversible capacity for those samples, an increase in the amount of Co^{4+} in the samples was observed with increasing upper cutoff potential (*i.e.*, incomplete relithiation on discharge to 2.7 V). The presence of paramagnetic Co^{4+} is expected to result in both a shift of the ^{27}Al resonance as well as a decrease in the spin-lattice (T_1) and spin-spin (T_2) relaxation times of the ^{27}Al nuclei. In the initially acquired ^{27}Al NMR spectra for each cycled sample, a very broad paramagnetic signal centered at 60 ppm was also observed, which is ascribed to ^{27}Al sites in close proximity to Co^{4+}, but not adjacent, since no significant hyperfine shift was observed.[10] The very broad signal could be suppressed by using a T_2 filter, and this method was used to acquire the spectra presented in Figure S17. A comparison showing the difference between non-filtered and T_2-filtered spectra is presented in Figure S18.

Figure S17 shows an increase in the intensity of the lower-frequency octahedral Al features, relative to the higher-frequency sharper signals, as the material is charged to higher voltages, indicative of the increased amount of Co^{4+} (*i.e.*, decrease in Co^{3+} content). The increased Co^{4+} content also appears to broaden the octahedral Al features, but the asymmetric increase of the overall lineshape due to the feature at ~70 ppm cannot be attributed to this broad signal. This higher-frequency feature falls in the characteristic 60–80 ppm range of Al in tetrahedrally coordinated environments.[11–13] Moreover, the signal is not attenuated by the T_2 filter and thus has a long T_2 relaxation time similar to the other diamagnetic Al features (*i.e.*, the resonances of the octahedral sites). On this basis, the fitted peak (broad, red peak) centered around 70 ppm is assigned to tetrahedral Al. Thus, the increase in intensity at higher frequencies is unrelated to changes in the octahedral Al sites or the increased Co^{4+} content, and instead indicates the development of tetrahedral Al. The intensity of the fitted tetrahedral Al peak clearly demonstrates that for $LiCo_{0.8}Al_{0.2}O_2$, Al migration to the tetrahedral site is observed even after charging to 4.2 V, and that the concentration of tetrahedral Al increases further when charging to higher potentials. In particular, a large increase in the tetrahedral Al peak is measured when charging above 4.5 V. These results can be contrasted to $LiNi_{0.8}Al_{02}O_2$ (O), for which no increase in the tetrahedral Al signal was observed even after charging to 4.75 V. As shown by the cycling results of the Al-substituted $LiCoO_2$ materials, the presence of tetrahedral Al will have a detrimental impact on the electrochemical performance of the positive electrode material. The presence of tetrahedral Al in between the CoO_2 layers presumably impedes the Li^+

diffusivity, as lower discharge capacities and higher irreversible losses are observed with increasing Al content in the $LiCo_{1-y}Al_yO_2$ electrodes.

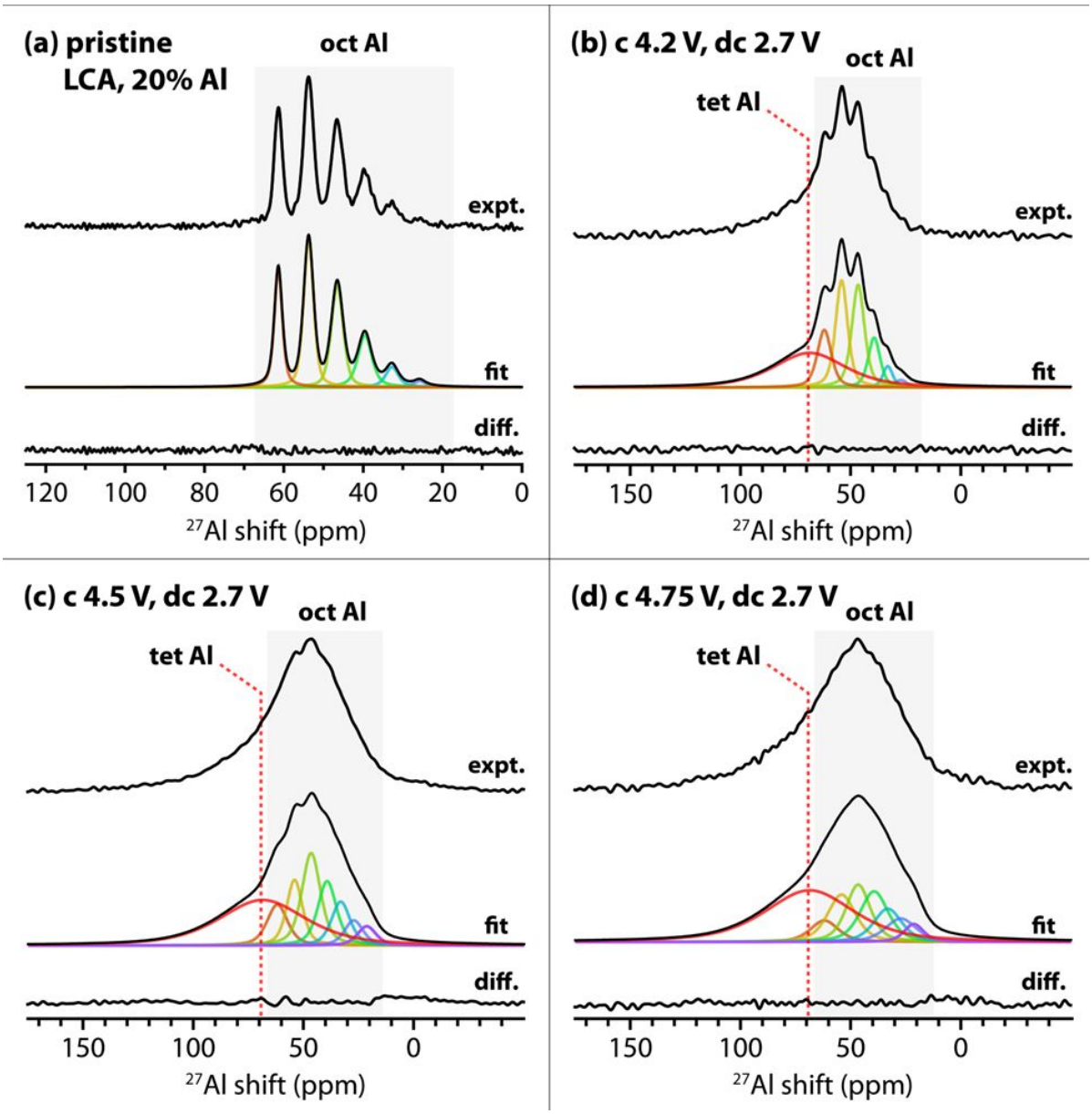

Figure S17: Experimentally measured and simulated ^{27}Al NMR spectra of (a) pristine $LiCo_{0.8}Al_{0.2}O_2$, as well as $LiCo_{0.8}Al_{0.2}O_2$ electrodes that were charged at 10 mA/g to (b) 4.2 V, (c) 4.5 V, or (d) 4.75 V and then subsequently discharged at 10 mA/g to 2.7 V. The octahedral (oct) Al peak locations were determined from the features observed in the spectrum of the pristine material, and correspond to Al sites with varying numbers of neighboring Co^{3+} ions. The positions of the octahedral Al features were fixed during the fitting procedure, and only the width of the octahedral Al peaks was varied when fitting the spectra of the cycled samples. In fits to the cycled spectra, a broad peak at 70 ppm was introduced and assigned to tetrahedral (tet) Al. The increased intensity of the lower-frequency octahedral sites is attributed to the increasing amount of Co^{4+} (decrease in Co^{3+} content) and is consistent with the electrochemical results, *i.e.*, incomplete relithiation. The relative intensity of the tetrahedral and octahedral peaks is not quantitative; the fit is presented primarily as a visual aid to show the tetrahedral Al feature.

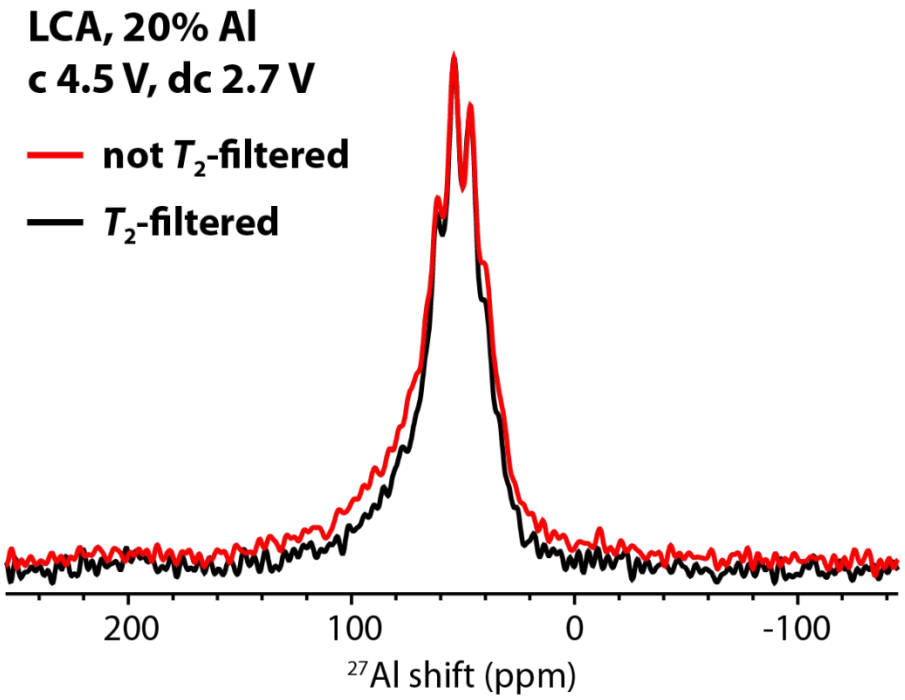

Figure S18: ^{27}Al solid-state NMR spectra of the cycled $LiCo_{0.8}Al_{0.2}O_2$ (LCA) sample charged to 4.5 V and then discharged to 2.7 V, showing an additional, extremely broad paramagnetic feature centered at ~60 ppm (in red spectrum). This paramagnetic feature could be suppressed through application of a T_2 filter, resulting in only the diamagnetic signals (black spectrum). The very broad signal is assigned to ^{27}Al sites in close proximity to Co^{4+}, or possibly ^{27}Al sites located in metallic regions of the sample. For both spectra, Hahn echo experiments were performed at a MAS rate of 55 kHz, at a field strength of 11.7 T. In the T_2-filtered spectrum, the length of the T_2 filter was 10 rotor periods, *i.e.*, the interpulse delay in the Hahn echo experiment was ~182 µs.

References:

(1) Croguennec, L.; Shao-Horn, Y.; Gloter, A.; Colliex, C.; Guilmard, M.; Fauth, F.; Delmas, C. Segregation Tendency in Layered Aluminum-Substituted Lithium Nickel Oxides. *Chem. Mater.* **2009**, *21*, 1051–1059.

(2) Jang, Y.; Huang, B.; Wang, H.; Sadoway, D. R.; Ceder, G. $LiAl_yCo_{1-y}O_2$ ($R\bar{3}m$) Intercalation Cathode for Rechargeable Lithium Batteries. *J. Electrochem. Soc.* **1999**, *146*, 862–868.

(3) Julien, C.; Nazri, G. A.; Rougier, A. Electrochemical Performances of Layered LiM1−yMy'O2 (M=Ni, Co; M'=Mg, Al, B) Oxides in Lithium Batteries. *Solid State Ionics* **2000**, *135*, 121–130.

(4) Rougier, A.; Saadoune, I.; Gravereau, P.; Willmann, P.; Delmas, C. Effect of Cobalt Substitution on Cationic Distribution in $LiNi_{1-y}Co_yO_2$ Electrode Materials. *Solid State Ionics* **1996**, *90*, 83–90.

(5) Kang, K.; Ceder, G. Factors That Affect Li Mobility in Layered Lithium Transition Metal Oxides. *Phys. Rev. B - Condens. Matter Mater. Phys.* **2006**, *74*, 1–7.

(6) Seguin, L.; Amatucci, G.; Anne, M.; Chabre, Y.; Strobel, P.; Tarascon, J. M.; Vaughan, G. Structural Study of NiO_2 and CoO_2 as End Members of the Lithiated Compounds by in Situ High Resolution X-Ray Powder Diffraction. *J. Power Sources* **1999**, *81–82*, 604–606.

(7) Tarascon, J. M.; Vaughan, G.; Chabre, Y; Seguin, L; Anne, M.; Strobel, A. P.; Amatucci, G. In Situ Structural and Electrochemical Study of $Ni_{1-X}Co_XO_2$ Metastable Oxides Prepared by Soft Chemistry. *J. Solid State Chem.* **1999**, *147*, 410–420.

(8) Momma, K.; Izumi, F. VESTA 3 for Three-Dimensional Visualization of Crystal, Volumetric and Morphology Data. *J. Appl. Crystallogr.* **2011**, *44* (6), 1272–1276.

(9) Gaudin, E.; Taulelle, F.; Stoyanova, R.; Zhecheva, E.; Alcántara, R.; Lavela, P.; Tirado, J. L. Cobalt(III) Effect on ^{27}Al NMR Chemical Shifts in $LiAl_xCo_{1-x}O_2$. *J. Phys. Chem. B* **2001**, *105* (34), 8081–8087.

(10) Trease, N. M.; Seymour, I. D.; Radin, M. D.; Liu, H.; Liu, H.; Hy, S.; Chernova, N.; Parikh, P.; Devaraj, A.; Wiaderek, K. M.; et al. Identifying the Distribution of Al^{3+} in $LiNi_{0.8}Co_{0.15}Al_{0.05}O_2$. *Chem. Mater.* **2016**, *28* (22), 8170–8180.

(11) Dupree, R.; Lewis, M. H.; Smith, M. E. Structural Characterization of Ceramic Phases With High-Resolution ^{27}Al NMR. *J. Appl. Crystallogr.* **1988**, *21*, 109–116.

(12) Madani, A.; Aznar, A.; Sanz, J.; Serratosa, J. M. ^{29}Silicon and ^{27}Aluminum NMR Study of Zeolite Formation from Alkali-Leached Kaolinites: Influence of Thermal Preactivation. *J. Phys. Chem.* **1990**, *94* (2), 760–765.

(13) Singh, P. S.; Trigg, M.; Burgar, I.; Bastow, T. Geopolymer Formation Processes at Room Temperature Studied by ^{29}Si and ^{27}Al MAS-NMR. *Mater. Sci. Eng. A* **2005**, *396* (1–2), 392–402.